



**HAL**  
open science

## Influence of the temperature on the opto-acoustophoretic effect

Gabriel Dumy, Mauricio Hoyos, Jean-Luc Aider

► **To cite this version:**

Gabriel Dumy, Mauricio Hoyos, Jean-Luc Aider. Influence of the temperature on the opto-acoustophoretic effect. *Journal of the Acoustical Society of America*, 2021, 149 (1), pp.556-568. 10.1121/10.0003058 . hal-03433272

**HAL Id: hal-03433272**

**<https://hal.science/hal-03433272>**

Submitted on 17 Nov 2021

**HAL** is a multi-disciplinary open access archive for the deposit and dissemination of scientific research documents, whether they are published or not. The documents may come from teaching and research institutions in France or abroad, or from public or private research centers.

L'archive ouverte pluridisciplinaire **HAL**, est destinée au dépôt et à la diffusion de documents scientifiques de niveau recherche, publiés ou non, émanant des établissements d'enseignement et de recherche français ou étrangers, des laboratoires publics ou privés.

## Influence of the temperature on the opto-acoustophoretic effect

Gabriel Dumy,<sup>1, a)</sup> Mauricio Hoyos,<sup>1</sup> and Jean-Luc Aider<sup>1</sup>

*Laboratory PMMH, ESPCI Paris PSL, Sorbonne Université*

1 Opto-acoustophoretic mobility has been demonstrated recently for fluorescent and  
2 colored particles acoustically levitated in a stationary ultrasonic field, when illumi-  
3 nated with the appropriate optical wavelength<sup>1,2</sup>. It is a repeatable phenomenon,  
4 needing both acoustic trapping and specific optic excitation to occur. However, the  
5 physical origin of the phenomenon is still debated. In this study, we provide more  
6 insights into the probable origin of this phenomenon, by confronting numerical sim-  
7 ulations with temperature controlled experiments. The phenomenon properties are  
8 well reproduced by our model relying on a thermofluidic instability, hinting at the  
9 potential thermally-induced fluid density gradient as a drag source for the observed  
10 ejection of particles. Thermostated experiments exhibit a surprising threshold, above  
11 which the phenomenon is not observed anymore, no matter how large the optic or  
12 acoustic energies used. This exciting new observation differs from the initial inter-  
13 pretation of the phenomenon, altering its potential application without removing its  
14 interest, since it suggests the possible contact-less generation of customized flows by  
15 acoustically trapped particles.

---

<sup>a)</sup> Also at Paris Descartes, University de Paris; [dumy.gabriel@gmail.com](mailto:dumy.gabriel@gmail.com)

## 16 I. INTRODUCTION

17 Waves can exert forces on scattering objects. This can be observed experimentally every  
18 time a comet crosses our skies, its tail effectively blown away by the radiative pressure exerted  
19 on these lone bodies by the electromagnetic waves coming from the sun, showing avid eyes  
20 that invisible things indeed could act on the material world. Ever since, evidence after  
21 evidence has been brought up by research on electromagnetic waves, eventually producing  
22 extremely useful techniques for life sciences such as optical tweezers<sup>3,4</sup>. More recent works  
23 have focused on the forces stemming from acoustic waves, and a large amount of research  
24 is dedicated to reach the potential already achieved by optical tweezers with their acoustic  
25 counterpart<sup>5-7</sup>.

26 It is quite usual now to use surface acoustic waves (SAW) or bulk acoustic waves (BAW)  
27 to build acoustic sorting devices or traps. The migration of acoustic-scattering particles in a  
28 standing acoustic wave, or acoustophoresis, has been used for over a decade to trap spherical  
29 particles in very specific locations of space, in order to study their mechanical properties<sup>8-10</sup>,  
30 and high hopes are given to grow cellular cultures while in acoustic levitation<sup>11-14</sup>. While  
31 acoustofluidics has been extensively explored in standard conditions, especially when applied  
32 to spherical rigid particles, there are still unknown phenomena discovered when applying  
33 acoustofluidics to other objects or in non-standard conditions. For instance, when the spher-  
34 ical symmetry assumption of the manipulated objects is no longer satisfied, such as with  
35 disks<sup>15</sup> or metallic micro-cylinders<sup>16-20</sup>, particles are actively propelled by the acoustic forces  
36 instead of quietly aggregating into stable positions. Unexpected effects can also arise when

37 using particles with specific properties, such as hollow core particles<sup>21,22</sup> or specific optical  
 38 properties<sup>1</sup>, which is the present study object.

39 The usual expression for the acoustic radiation force (ARF) experienced by spherical  
 40 particles suspended in a liquid medium in a purely transverse standing wave ultrasonic  
 41 acoustic field, along the direction of propagation of said field, can be derived following the  
 42 Gor'kov approach<sup>23</sup>:

$$\mathbf{F}_{ac}(z) = \frac{\pi}{2} \langle E_{ac} \rangle k d_p^3 F_Y \sin(2 k_{ac} z) \mathbf{e}_z \quad (1)$$

43 where  $\langle - \rangle$  denotes time averaging,  $d_p$  is the particle diameter,  $\langle E_{ac} \rangle$  is the time-averaged  
 44 acoustic energy density inside the channel,  $k = \frac{2\pi}{\lambda_{ac}} = \frac{2\pi f_{ac}}{c}$  is the wave number of the  
 45 acoustic plane wave of frequency  $f_{ac}$ , and  $z$  is the axial (or vertical) position of the particle,  
 46  $z = 0$  being at the bottom of the channel and  $z = h$  being at the top. This expression  
 47 can be corrected for fluid viscosity or particle elasticity<sup>24-26</sup>. However, we will neglect fluid  
 48 viscosity corrections, since the particles in this study are always 5 micrometer in diameter  
 49 or more, much larger than the viscosity length of 400 nm (at 20°C for a 2.0 MHz acoustic  
 50 wave in water).

51 The acoustic contrast factor  $F_Y$  of a given particle of density  $\rho_p$  in a medium of density  
 52  $\rho_f$ , exposed to an acoustic wave propagating at  $c_f$  in the medium and at  $c_p$  in the particle,  
 53 is then defined as:

$$F_Y = \frac{1 + \frac{2}{3} \left(1 - \frac{\rho_f}{\rho_p}\right)}{2 + \frac{\rho_f}{\rho_p}} - \frac{\rho_f c_f^2}{3 \rho_p c_p^2} \quad (2)$$

54 Depending on the sign of the acoustic contrast factor, the suspended objects will move  
 55 toward the pressure node or pressure anti-node of the acoustic field. Negative contrast  
 56 factors object can be found amongst bubbles, or specific lipid droplets for instance. In this  
 57 study we consider only objects with positive contrast factors (such as plastic particles or red  
 58 blood cells), indeed moved toward the pressure node (Fig. 1a) where they will be kept in  
 59 acoustic levitation (Fig. 1b and c). The particles equilibrium position is called the levitation  
 60 plane, and is a result of the competition between buoyancy, gravity and acoustic forces<sup>27</sup>.

61 The radial component of the ARF may be neglected in many applications like acoustic  
 62 sorting because it is usually one order of magnitude weaker than the axial component<sup>28,29</sup>.  
 63 Nevertheless it plays a crucial role in closed cavities, once the particles have reached the  
 64 levitation plane. Following<sup>7</sup>, the transverse component of the ARF inside the levitation  
 65 plane can be expressed as:

$$\mathbf{F}_T(x, y) = d_p^3 \frac{3(\rho_p - \rho_f)}{\rho_f + 2\rho_p} \nabla \langle E_{ac} \rangle (x, y) \quad (3)$$

66 This component depends directly upon the radial gradient of the acoustic energy  
 67  $\nabla \langle E_{ac} \rangle (x, y)$  and is responsible for the aggregation of particles toward the local maxi-  
 68 mum of acoustic energy in the levitation plane (Fig. 1c). It is mainly defined by the shape  
 69 of the acoustic energy density landscape, which is related to the source of the ultrasonic  
 70 wave and to the geometry, materials and boundary conditions of the resonant cavity.

71 These equations describe correctly the forces applied to spherical particles made of soft  
 72 or rigid materials, such as polymers, silica, or biological materials, either passive (e.g. red  
 73 blood cells), or active (e.g. bacteria<sup>14</sup> that can extract and convert chemical energy available

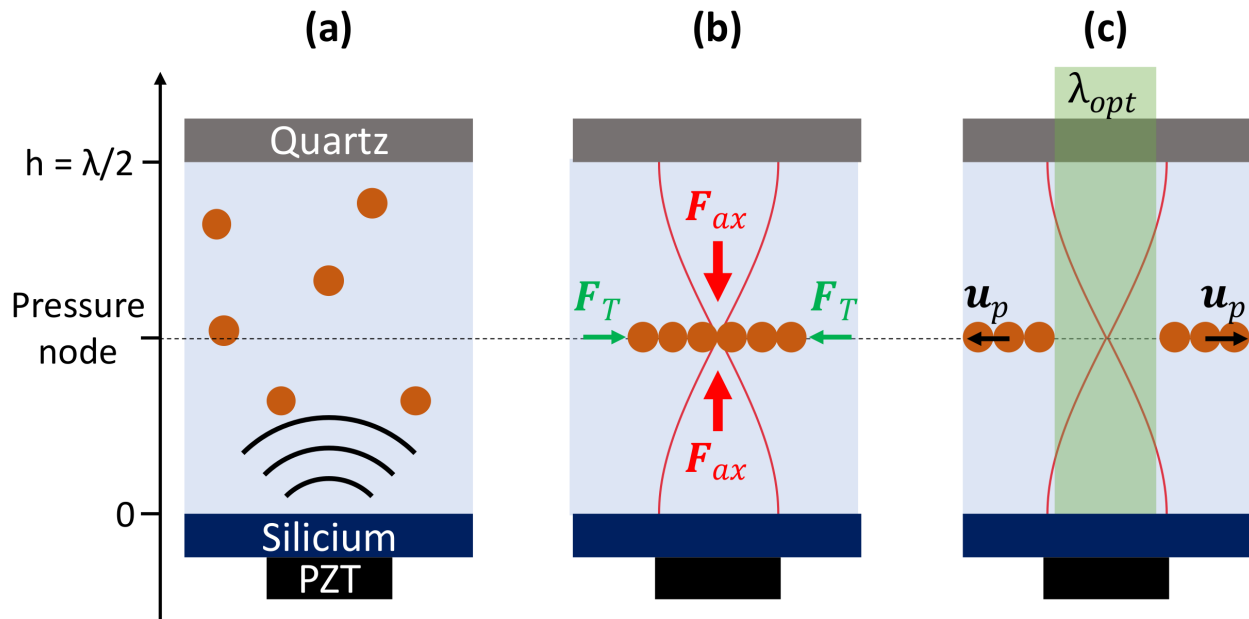


FIG. 1. (a) Sketch of the acoustic resonant cavity filled with a micrometric particle suspension (side view). A silicium wafer with a piezoelectric transducer attached makes the cavity floor, while the top wall is a quartz lid allowing good optical access for both observation and illumination. If the cavity height and the acoustic frequency are properly tuned, then the ultrasounds emitted by the transducer will build a standing wave profile, with a pressure node at cavity mid-height. (b) The particles gather at the pressure node under the ARF (both components illustrated) where they can be kept in acoustic levitation, away from the walls. (c) If the particles are enlightened with the proper optical wavelength, they can be laterally expelled from the illuminated area, while still kept in acoustic levitation.

74 to them into motion or forces, i.e. kinetic and potential energies). Recently, it has been  
 75 shown that the acoustic focusing and aggregation process of passive particles trapped in an  
 76 ultrasonic field could be affected by an illumination at specific optical wavelength<sup>1</sup>. Instead

77 of being trapped and aggregated into a stable position of space (acoustic trapping), the levi-  
78 tated particles, if enlightened with a proper wavelength, could be radially expelled from their  
79 equilibrium aggregation position, while staying confined into the levitation plane (Fig. 1d).  
80 The phenomenon is robust and has been demonstrated for different types of fluorescent or  
81 coloured particles. A clear dependency to the amplitude of the acoustic wave as well as to  
82 the power of the light source has been found. The coupling of both actuation is needed.  
83 Different hypotheses have been raised but no definitive explanation could be assessed.

84 The objective of this study is to investigate a thermal origin of the phenomenon. After  
85 a short description of the experimental setup, we will present an temperature controlled  
86 experiment to assess an idea inspired by a recent extension of the classical acoustophoresis  
87 development to fluids particles<sup>30</sup>. Finally, since the main argument of this explanation  
88 rises from a thermo-acoustofluidic effect, numeric simulations are presented, enriching the  
89 discussion about the optoacoustofluidic effect generation.

## 90 II. MATERIALS AND METHODS

### 91 A. Acoustic cavity

92 In this study we use the same circular aluminium acoustic cavities as the one used in the  
93 previous study<sup>1</sup>. It consists of an in-house aluminum body, holding the different components  
94 of the device and constituting the walls of the resonant cavity. The inner dimensions of the  
95 cavity are defined by its diameter  $D = 20$  mm and its height  $h = 800$   $\mu\text{m}$ . The height can  
96 be tuned to match the half-wavelength of the acoustic field  $\lambda_{ac} = 2h$  (see Fig. 2 a-c).

97 In this setup, the resonant frequency maximizing the acoustic effects is found to be around  
 98  $f_{ac} \simeq 737$  kHz under ambient conditions. The lower wall of the cavity is a silicone wafer  
 99 (thickness  $h_{trans} = 0.30$  mm), onto which is glued a piezoelectric ceramic PZT26 (Ferroperm-  
 100 Meggit<sup>TM</sup>, disk ceramic, 2 mm thick, 15 mm wide, nominal resonant frequency 1MHz) with  
 101 a water soluble glue. The top of the cavity is closed with a  $h_{ref} = 1.1$  mm thick quartz  
 102 disc (High Tech Materials<sup>TM</sup>), which is both a good acoustic reflector and a good optical  
 103 transmitter, allowing good optical access for microscopy observations inside the cavity. The  
 104 position of the quartz lid is guaranteed against surface tension by another ring of aluminium,  
 105 that is held flat against the quartz with two elastic bands (see Fig. 2 (d) for a global view  
 106 of the device).

107 The PZT is powered by a all-in-one wave generator and oscilloscope combo (TiePie<sup>TM</sup>  
 108 Handyscope HS5) allowing the variation of the applied voltage between a few mV to more  
 109 than 10 V peak to peak.

110 It is often more convenient to speak of the acoustic energy density carried by the acoustic  
 111 standing field in order to compare rigorously different experiments. A calibration is made in  
 112 our cavity to link  $\langle E_{ac} \rangle$ , measured by the method proposed by<sup>31</sup>, with the amplitude of the  
 113 electric voltage applied to the PZT. The principle consists in measuring the axial focusing  
 114 velocity of a known particle for a given voltage to deduce the acoustic force, yielding a value  
 115 for the acoustic energy.

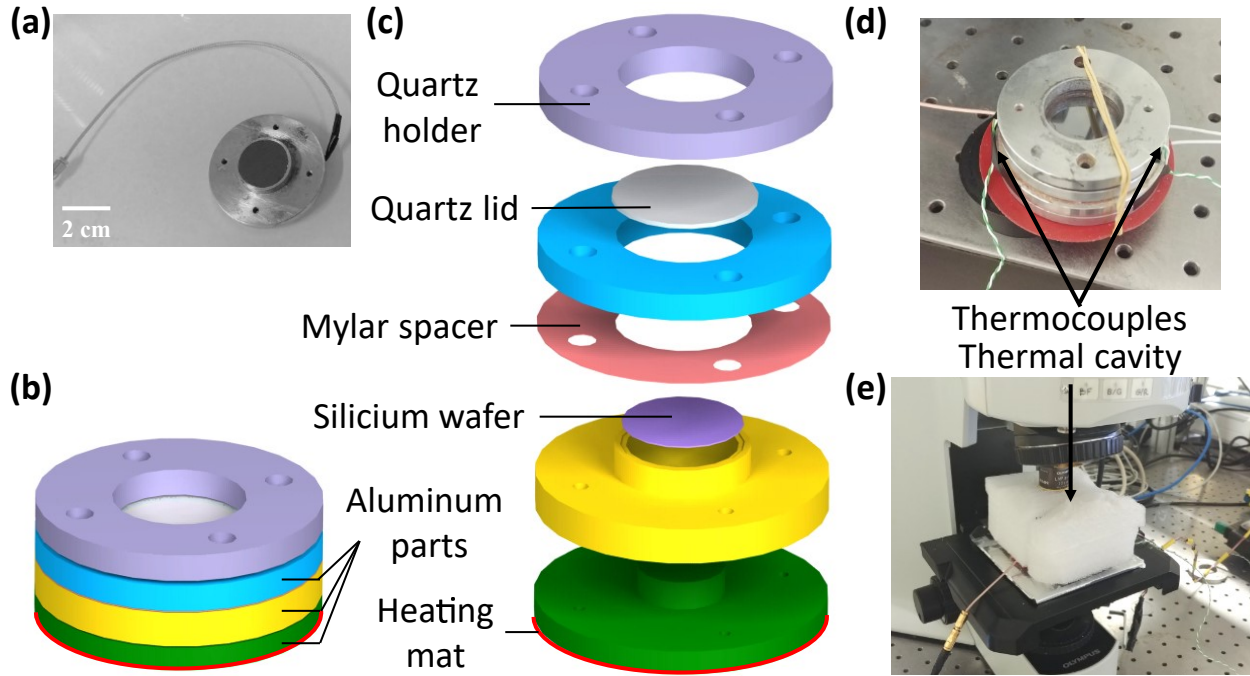


FIG. 2. (a) Picture of the aluminium cavity. (b) Assembled and (c) exploded views of the setup. The aluminium body is made of three aluminium parts: one (yellow) holding a silicon wafer on top of it, another (blue) fitting it and constituting the walls of the cavity. The relative height of resonant cavity is controlled by the insertion of one or several Mylar layers in-between. A piezoelectric transducer (PZT) is glued under the silicon wafer, soldered to a BNC cable. A (green) bottom part closes the device while allowing for cable fitting. A heating mat is stuck under this last part for thermal experiments. The whole device is tightened with screws, and the cavity is closed with a quartz lid held on top of it by an optional second aluminium ring (light grey). (d) View of the thermal acoustic resonator and (e) of the resonator inserted into the insulated chamber fixed on the moving stage of the microscope.

116 **B. Thermal setup**

117 In order to control the temperature of the system, we add to our device two elements: a  
 118 heat source and a thermal isolation. The heat source is a disc-shaped heating silicon mattress  
 119 (RadioSpares Pro, 4W output power), which is fixed under the aluminium structure. It is  
 120 connected to a continuous current power source, with a controllable output (RadioSpares  
 121 Pro). The acoustic cavity has to be isolated from the laboratory air convection, but also to  
 122 minimize the heat loss. To keep an optical access to the cavity from the top, the aluminium  
 123 cavity has been inserted inside a carved box made of polyester foam, covered on the inside  
 124 by a layer of aluminium paper, to keep in also the radiated heat from the device (Fig. 2e).

125 The aluminium structure temperature could then be monitored using two thermocouples  
 126 (K type thermocouples connected to a Hanna Instruments HI92804C logging box) that were  
 127 stuck on the quartz lid sides, where it is easier to get a measurement. We also used a real-  
 128 time Arduino-based logging device with a generic TMP36GT9Z thermosensor, held down on  
 129 the silicon wafer center for calibration measurements. The data have been used to measure  
 130 the dynamic thermal evolution of the cavity, as well as calibrating the slight gap between  
 131 the two thermocouples placed outside of the cavity and its center.

132 Several time-evolutions of the silicon wafer temperature were recorded for different ther-  
 133 mal powers of the heating mattress and fitted with a simple exponential:

$$T(t) = \alpha \times (1 - e^{-t/\tau}) \quad (4)$$

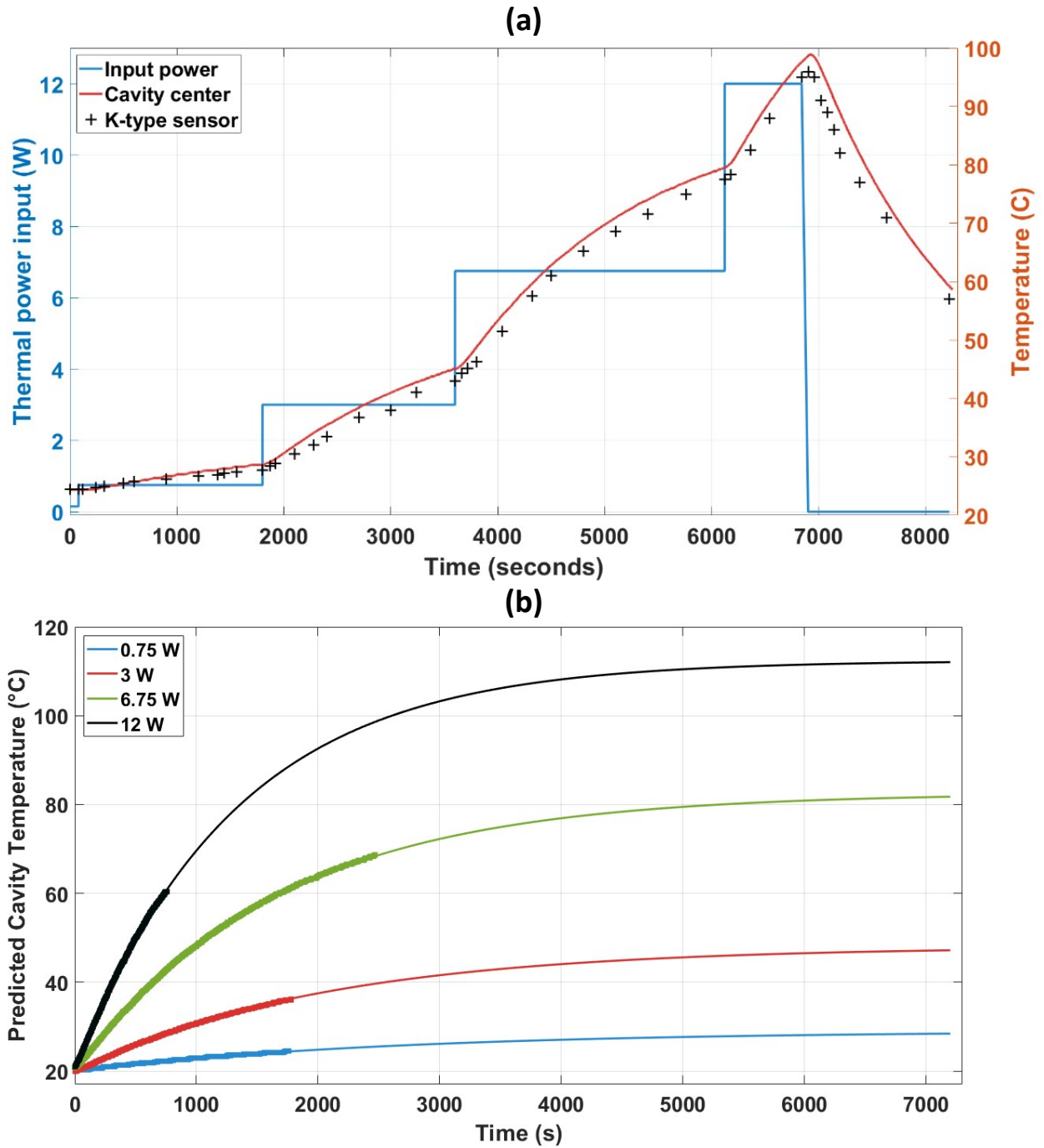


FIG. 3. a) Evolution of the temperature at the center of the silicone wafer as a function of time, for increasing heating powers. b) The temperature evolution for different powers are used to calibrate the thermal response of the setup. Each curve can be fitted with an exponential. Once the dynamic thermal response as a function of the input power is calibrated, it is possible to predict the temporal response of the cavity with the imposed power.

134 Once the evolution of  $\alpha$  and  $\beta = 1/\tau$  with the thermal power is known, it is possible to  
 135 use it as a calibration to predict the cavity temperature as a function of the applied thermal  
 136 power (Fig. 3b).

137 We can also compare the real-time evolution of the thermosensor output with discrete  
 138 measurements obtained with the thermocouple. As we can see on Fig. 3a, the thermosensor  
 139 measures a slightly higher temperature, which can be explained by an inhomogeneity of the  
 140 heat distribution as well as the difference in thermal conductivity paths leading to the two  
 141 measurement points.

### 142 C. Calibration of the acoustic properties of the heated cavity

143 Heating the fluid has various consequences, especially for the acoustics, which have to be  
 144 taken into account. Heating the fluid changes its density and compressibility, which implies  
 145 a change of the acoustic contrast factor (eq. 2). However, even for an unrealistic  $\Delta T$  of 80  
 146 K,  $F_Y$  undergoes a relative variation approximating  $10^{-5}$ , that we will neglect.

147 The second effect is a modification of the sound velocity in addition to a dilatation of the  
 148 cavity, affecting the acoustic resonance. For each temperature increase, the new acoustic  
 149 resonant frequency has been measured by looking for the reflected electric signal minimum,  
 150 which is a signature of the cavity electromechanical resonance. This way we aim to avoid  
 151 any errors due to an uncontrolled frequency drift induced by the temperature. Resonant  
 152 frequency shifted during the experiment from 735 kHz at 20°C to 772 kHz at 70°C, a relative  
 153 variation of 4.7%, correction which is not negligible and the resonant cavity detuning is then  
 154 avoided by adjusting the frequency applied to the PZT.

#### 155 **D. Optical setup**

156 The observations are made through the top quartz lid, along the axis of propagation of  
157 the acoustic waves, using a reflection microscope (Olympus BX-2<sup>TM</sup>), as shown on Fig. 2e.  
158 The samples are illuminated by a LED source (CoolLED pE-4000<sup>TM</sup>) allowing a very good  
159 control of the optical wavelength  $\lambda_{opt}$  (16 different wavelengths between 360 nm and 800  
160 nm) and power of illumination. A 80% reflective optical filter has been added to the filter  
161 cube. Most of the observations were made using a PCO Panda 4.2bi camera at 40 fps, when  
162 not indicated otherwise. The quantitative measurements were made using a PCO Dimax  
163 CS3<sup>TM</sup> fast camera at 100 fps, to allow a better tracking of the particles. Snapshots were  
164 post-treated (contrast improvement, definition of the ROI) with the free software ImageJ  
165 (<https://imagej.nih.gov/ij/>). The power delivered by the CoolLED to the resonant  
166 cavity has been measured at the focus of the microscope objectives using a ThorLabs PM16-  
167 130 Probe (Spectral range 400 to 1100 nm, 1 cm  $\times$  1 cm silicon sensor area, optical power  
168 range 5 pW - 500 mW) connected to a computer.

#### 169 **E. Measurements of the ejection velocity**

170 In a previous study<sup>1</sup>, the optoacoustofluidics effect was quantified through the slope of a  
171 time projection of the aggregate expansion. It gives a good estimate of the global effect of  
172 the sudden illumination of an aggregate through its outer boundary ejection velocity.

173 In this study we improved our measurement technique by using a particle tracking algo-  
174 rithm to measure the velocity of ejected particles. This algorithm was initially developed by

175 the Environmental Complexity Lab, Stanford University, USA<sup>32,33</sup>. The available algorithms  
 176 have been parallelized and tailored to fit our snapshots time-series.

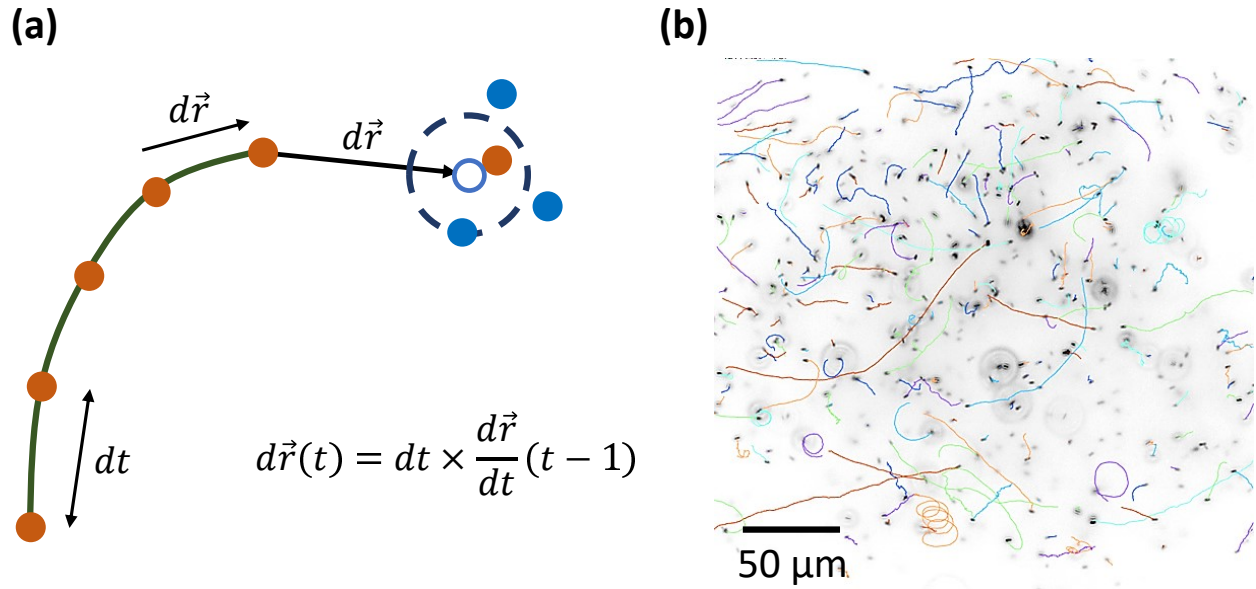


FIG. 4. (a) Sketch of the particle tracking algorithm. A particle is tracked along its trajectory. At the time step  $t$ , all the local particles have been spotted. To reconnect the "correct" one to the track we are following, we compute the estimated  $d\vec{r}$  the particle should have moved during  $dt$ . Then the closest particle to this guessed position found in the following snapshot ( $t + dt$ ) is affected to the track. (b) Example of the simultaneous tracking of a collection of pure Au nanorods propelled by the ARF and moving with ballistic trajectories inside the levitation plane (1.84 MHz,  $\langle E_{ac} \rangle \simeq 70 \text{ J.m}^{-3}$ , velocities around  $100 \mu\text{m.s}^{-1}$ ).

177 The method consists in a two-step iterative process:

- 178 1. All the particles in all the data frames are spotted, according to a threshold's param-  
 179 eters set by the user,
- 180 2. Tracks themselves are built by connecting particle positions from frame to frame.

181 To allocate a particle to a given track  $T_n$  at  $t + dt$ , the routine establishes a guess for the  
182 most probable position for the particle at  $t + dt$  based on its history at  $t, t - dt$ , and so on.  
183 Then it links to the track  $T_n$  the particle that minimizes the most the cost function defined  
184 as the squared distance between the particle position and this most probable position, as  
185 sketched on Fig. 4 a).

186 The frame rate of the camera is high enough to follow every change in direction of the  
187 moving particles. Once the acoustic force is activated, the Brownian motion becomes usually  
188 negligible for our particles (larger than  $1 \mu\text{m}$ ) leading to a robust prediction of their positions  
189 in most of the cases.

190 Once the particle tracks are recorded from an image sequence of a movie file, they are  
191 post-processed according to their quality: noisy data will be filtered by applying a moving  
192 average over the positions (generally using a 3 to 5 time-steps averaging), a critical length  
193 will be defined for each experiment under which the tracks will be considered as irrelevant,  
194 and outliers/parasitic data will be removed from the set.

### 195 **III. OPTOACOUSTOPHORESIS**

196 The phenomenon of acoustic trapping is well understood theoretically for spheres, and its  
197 various experimental applications have been extensively covered. Recently, we have shown  
198 that if an aggregate of spherical particles in acoustic levitation was illuminated with a proper  
199 optical wavelength  $\lambda_{opt}$  with enough power, then the particles are quickly ejected from the  
200 illuminated area, while still in acoustic levitation. Indeed, the particles exit the aggregation  
201 area radially, while staying focused when observed from the top (see Fig. 5, b and c), meaning

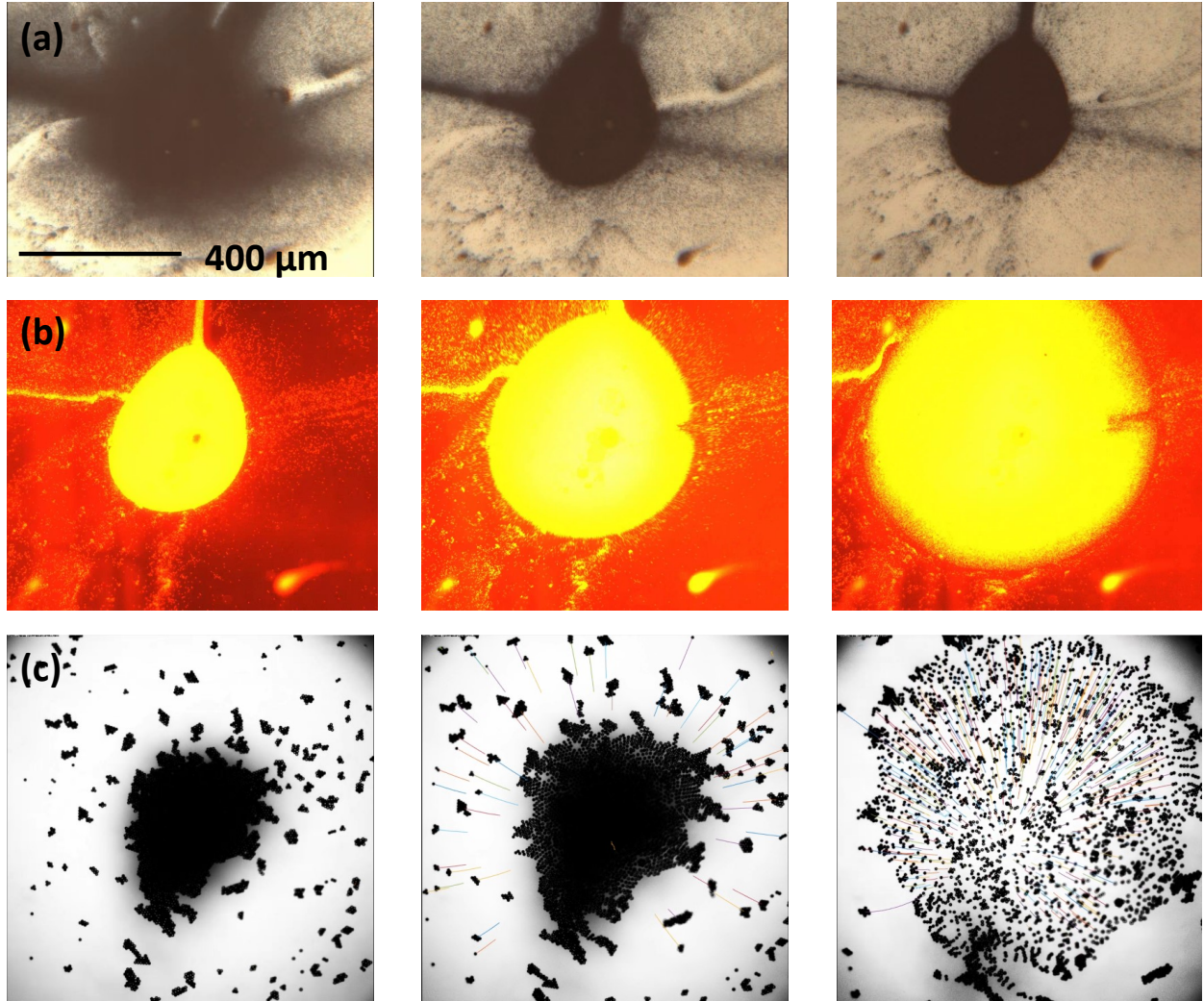


FIG. 5. (a) Illustration of a standard radial aggregation of particles in the acoustic pressure node, for 1.62  $\mu\text{m}$  polystyrene particles in a 1.82 MHz acoustic field. A large aggregate is formed and can be maintained as long as needed in acoustic levitation. (b) If the aggregate is illuminated by a strong green ( $\lambda_{opt} = 545 \text{ nm}$ ) light, then the red fluorescent particles, absorbing the green light, are violently ejected from the illuminated area. (c) This "opto-acoustofluidic" effect has also been observed for colored particles (here 10  $\mu\text{m}$  red colored polystyrene particles), demonstrating that the fluorescence is not needed. Only light absorption is necessary (maximum effect at  $\lambda_{opt} = 550$  or 580 nm). We show particles trajectories superimposed to the snapshots.

202 that the  $z$  displacement is less than the objective depth of field, i.e. 5  $\mu\text{m}$ . They are ejected  
203 toward the illuminated area frontier where they can aggregate again. The ejection velocities  
204 can be as high as few hundreds times their diameter per second.

205 We illustrate on Fig. 5 c) the disaggregation of a large aggregate of particles at different  
206 time steps, along with tracked trajectories measured using the algorithm described in the  
207 previous section.

208 The fact that particles are not ejected isotropically, but stay confined into the levitation  
209 plane, ruled out one origin for the phenomenon, i.e. a sign inversion of the acoustic contrast  
210 (Eq. 2). Indeed, if the illuminated particles were heating enough to change their material  
211 properties compared to the carrying fluid, then the acoustic contrast factor would change  
212 sign as well as all the acoustic force components. In this case we should also observe an axial  
213 expulsion from the aggregate, with the particles effectively fleeing away from the pressure  
214 node isotropically, which is not the case.

215 A very interesting result was found through a parametric evolution. Indeed it can only be  
216 observed with a strong coupling between the optical power and the acoustic energy carried  
217 by the acoustic field. The more optical power was used to illuminate the aggregate the  
218 stronger the desegregation, which could be expected. But the stronger the acoustic trap,  
219 the higher the ejection velocity, which is quite counter-intuitive. This result was reproduced  
220 with several sizes of particles, with the same effect for each experiment. It also ruled out a  
221 number of possible physical origins for the phenomenon.

222 **IV. EXPERIMENTAL INVESTIGATION OF A THERMAL EFFECT**

223 It has been shown recently that fluid layers with a relatively small contrast factor can  
 224 undergo ARF effects<sup>30</sup>. This is a side effect that can be a strong limitation to the separation  
 225 of particles transported in layers of fluid of different densities. One could also expect that  
 226 if the temperature of a particle  $T_{part}$  is increased and then becomes different from the sur-  
 227 rounding fluid, then a thermal boundary layer  $\delta_{therm}$  should be created around the particle,  
 228 or the aggregate of particles (Fig. 6). Increasing the temperature of the fluid leads to a  
 229 decrease of its density. It is then possible that the particles or aggregates of particles are  
 230 surrounded by a fluid layer with a density  $\rho_f(T_1)$  lower than the one of the surrounding fluid  
 231  $\rho_f(T_0)$ . Following the proposition of<sup>30</sup>, if two fluids of different densities are subjected to an  
 232 acoustic field of energy  $E_{ac}$ , then the fluids will undergo a volume force  $F_{ac-flu}$  defined as:

$$\mathbf{F}_{ac-flu} = -\cos(2ky) \cdot E_{ac} \nabla \tilde{\rho}_f \tag{5}$$

233 where  $\tilde{\rho}_f$  is the perturbation in fluid density. One can see that if there is a fluid density  
 234 gradient, then the fluid layer will undergo an acoustic force aligned with density gradients,  
 235 leading to a possible motion of the fluid layer. The lower density fluid shell surrounding the  
 236 particle may drag the particle radially, while the particle itself is still kept in acoustic levi-  
 237 tation by the primary axial acoustic force. The force applied to the fluid and corresponding  
 238 drag should be larger than the transverse component of the ARF applied to the particle to  
 239 pull the particle away from the aggregation site. The resulting ejection speed would then be

240 a competition between the transverse component of the acoustic force applied to the particle  
 241 and viscous drag imposed by the fluid layer moved by  $F_{ac-flu}$ .

### 242 **A. Acoustic instability of the thermal boundary layer**

243 The objective of these experiments is to assess the role played by possible thermal effects  
 244 on the opto-acoustofluidic effect. We will rule out a simple thermal convection effect in  
 245 Section V. One other hypothesis discussed in the previous study was based on successive  
 246 possible steps triggered when the particles are illuminated. We are interested in the thermal  
 247 heating of local fluid layers which will undergo a possible acoustic instability.

248 In any case, if the density gradient induced by local thermal heating is responsible of par-  
 249 ticle's ejection, then changing the surrounding fluid temperature should modify the ejection  
 250 process and ultimately, for a high-enough temperature, might cancel it. The objective of  
 251 following experiments is to check this hypothesis.

### 252 **B. Influence of the temperature on the ejection velocity**

253 For these experiments we used 10  $\mu\text{m}$  red dyed particles in the thermostated device  
 254 described in Section II A. Particle concentration was on the order of magnitude of  $1 \mu\text{g.mL}^{-1}$ ,  
 255 this concentration yielding for our observation conditions a reproducible aggregate with a  
 256 correct size. A constant acoustic voltage  $U = 2.6 V_{pp}$  is applied, while the particles are  
 257 illuminated at the same optical wavelength  $\lambda_{opt} = 550 \text{ nm}$  with the maximum power of the  
 258 CoolLED. For each temperature, the acoustic frequency is tuned at the proper resonance

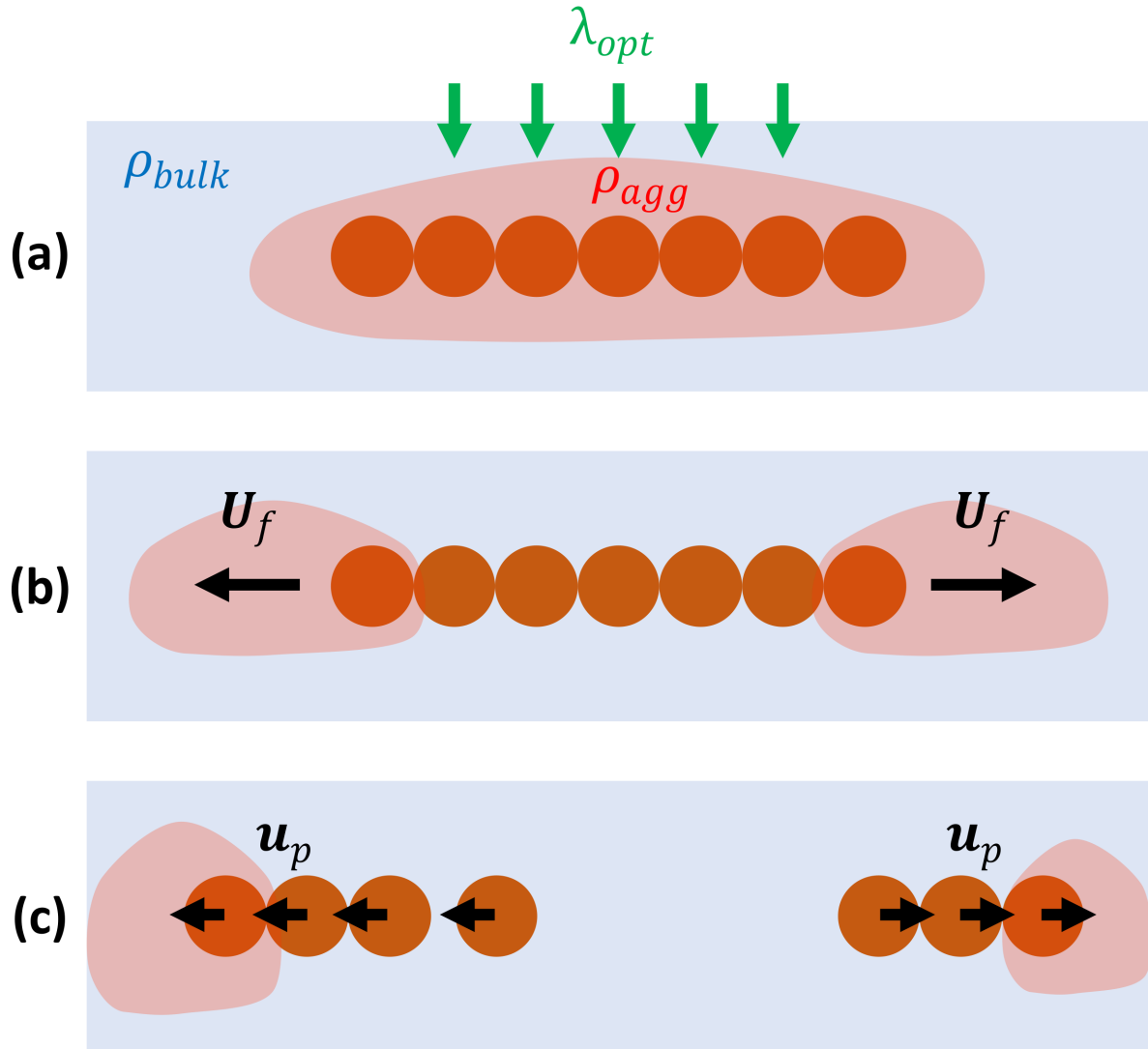


FIG. 6. Illustration of an aggregate who, once illuminated by a specific absorbed wavelength  $\lambda_{opt}$  might absorb the incident energy, therefore heating up the surrounding fluid, thus generating a thermal layer around it (a). The heated layer will then have a lower density than the cooler surrounding fluid, which might generate fluid motion by convection or acoustic instability (b). The particles would then undergo motion through Stokes drag, leading to the observed optoacoustofluidic explosions (c).

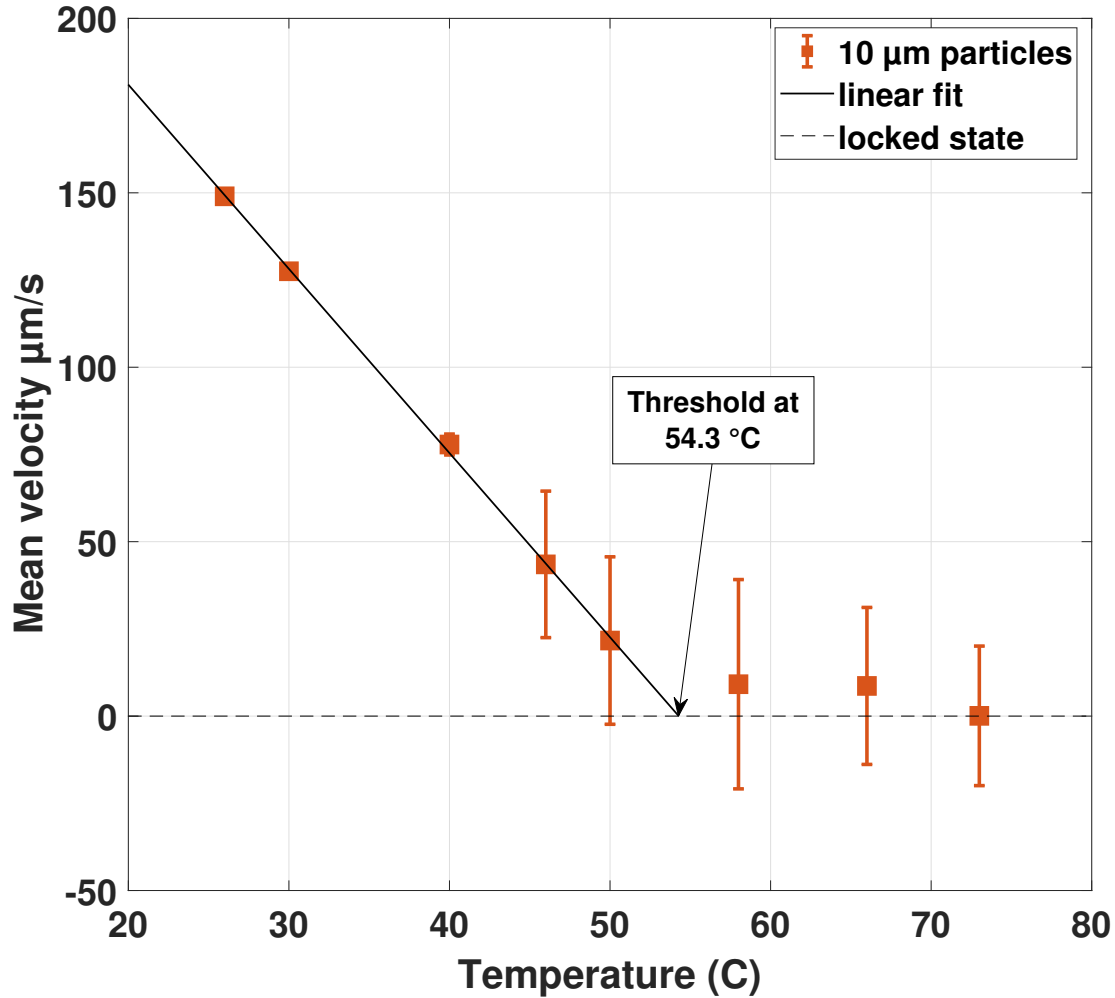


FIG. 7. Ejection velocity of 10  $\mu\text{m}$  red dyed polystyrene beads as a function of the temperature.

One can see that the ejection velocity is linearly decreasing down to a threshold temperature  $T_{crit} = 54.3^\circ\text{C}$ . For temperatures higher than  $T_{crit}$  the particles remain aggregated in acoustic levitation but no longer react to the illumination.

259 frequency. We record the particles expulsion when illuminated. An illustration of this

260 experiment is available as a movie : MM1: this is a movie of type "mp4" (9.67Mb).

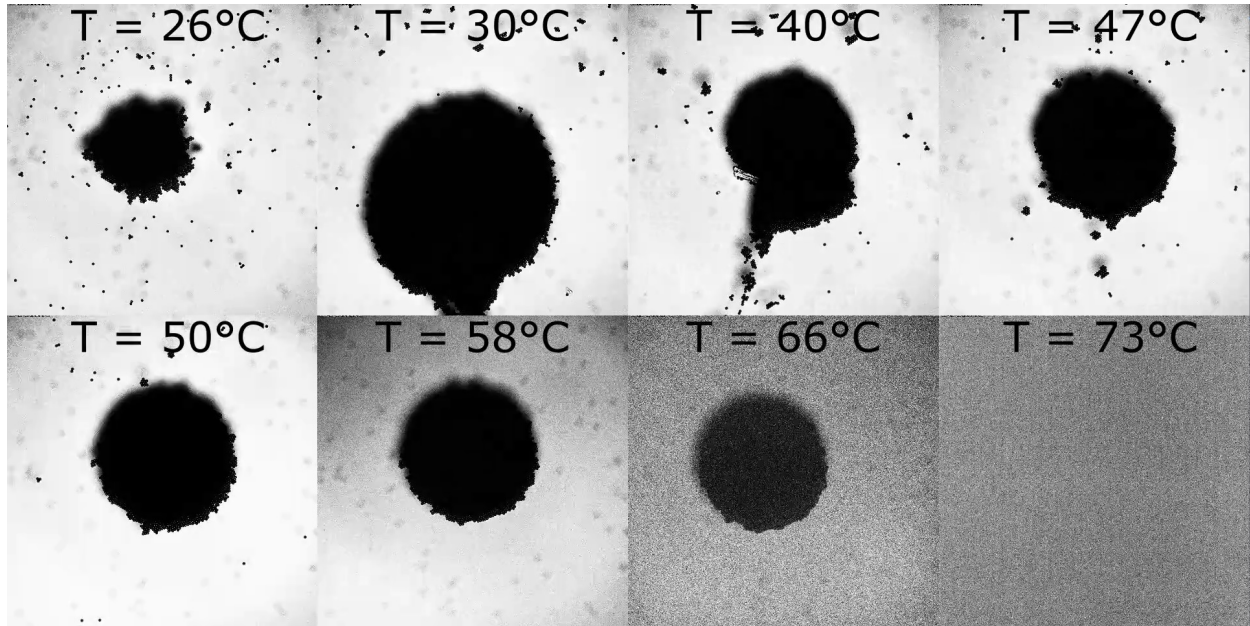


FIG. 8. Illustration of the temperature controlled experiment. 10  $\mu\text{m}$  red particles exposed to the same acoustic field and enlightened with the same optical wave are ejected from the aggregation area at different experiment temperatures. One can clearly see the process slowing with the temperature rise.

261 The trajectories obtained from the Lagrangian tracking of the particles are processed to  
 262 get their velocity as a function of time, which are then averaged over the number of tracked  
 263 particles. The results are summarized on Fig. 7. One can notice two interesting features.

- 264 1. Ejection velocity decreases linearly with increasing temperature
  
- 265 2. There exists a critical temperature above which the particles are no longer ejected  
 266 from the illuminated area, in this case 54.3°C.

267 It is important to note that since these experiments are also conducted at slightly different  
268 frequencies thanks to the cavity heating (as described in II C). When conducting control  
269 experiments at these frequencies but with  $T = 20^\circ\text{C}$ , the ejection was effective.

270 This results clearly demonstrate that the temperature difference between the bulk fluid  
271 and the heated layer surrounding the particles plays a critical role. Once the bulk fluid  
272 becomes hotter than the heated layer, the expulsion mechanism is turned off. This result  
273 is compatible with the idea of a heated fluid layer being pushed by the acoustic force. To  
274 check this theory, we carried out numerical simulations on simple configurations including  
275 the various forces playing a role in this phenomenon.

## 276 V. NUMERICAL INVESTIGATION

277 We present in this section numerical simulations that were conducted with Comsol Mul-  
278 tiphysics 5.1, in order to evaluate the effects of the heated layer surrounding a particle or an  
279 aggregate discussed previously. The simulations are used as a tool to have a better insight  
280 into the local effects discussed previously. We will see that small temperature gradients  
281 could generate large flows if the acoustic force is taken into account.

282 The main physical parameters used for the simulations are summarized in Table I.

283 All the simulations were performed on a DELL Precision 7820 tower computer running  
284 Windows 10 Professional for workstations (64 bits), equipped with with 64 GB of RAM and  
285 two Intel Xeon Bronze 3106 CPUs with 8 cores each, cadenced at 1.7 GHz and attached to  
286 11 MB of cache memory.

287 **A. Rayleigh-Bénard instability**

288 When dealing with thermal effects in fluids, the first question is whether or not the  
 289 fluid can undergo Rayleigh-Bénard instability. The previous experiment suggest a possible  
 290 temperature difference  $\Delta T \approx 35^\circ$  when running an experiments at room temperature (20°  
 291 C). In this case one should compute the Rayleigh number, defined as:

$$R_a = \frac{g\rho_f\alpha_w}{\nu D_{th}} \times \Delta T \cdot L^3 = G_r \times P_r \quad (6)$$

292 where  $G_r$  is the Grashof number and  $P_r$  is the Prandtl number.  $D_{th}$  is the thermal  
 293 diffusion coefficient,  $L$  the length scale over which the thermal gradient takes place,  $\alpha_w$  is  
 294 the thermal expansion coefficient and  $\nu$  is the kinematic viscosity.

295 Using the values of the various physical parameters summarized in Table I, it is possible  
 296 to compute extremes values of the Rayleigh number as a function of the temperature. Even  
 297 with unreasonable control parameters ( $\Delta T = 100$  degrees,  $L = 1$  mm yield  $R_a \simeq 10^3$ ) the  
 298 Rayleigh numbers remains lower than the critical value ( $R_a \leq R_a^{crit} = 1708$ ) above which  
 299 the thermal convection is triggered. The ejection of the particles when illuminated can not  
 300 be explained by a simple thermal convection effect.

301 **B. Geometry, boundary conditions and mesh definition**

302 As we are interested in evaluating the coupling effect of thermal heating and acoustic  
 303 entrainment, we neglect possible 3D effect and simplify the geometry of the experimental  
 304 setup. We use the cylindrical symmetry of the problem to model the cylindrical cavity as

TABLE I. Table summarizing the main physical parameters characterizing the fluid and the polystyrene particles. We used these parameters to compute the temperature dependency of the Rayleigh number as well as for the numerical simulations. We used the values of the COMSOL Material Library as well as their temperature dependence.

Polystyrene			
Density	$\rho_{ps}$	1060	$kg.m^{-1}$
Speed of sound	$c_{ps}$	2350	$m.s^{-1}$
Compressibility	$\beta_{ps}$	$2.48.10^{-10}$	$Pa^{-1}$
Water			
Density <sup>a</sup>	$\rho_w$	999	$kg.m^{-1}$
Speed of sound	$c_w$	1481	$m.s^{-1}$
Compressibility	$\beta_w$	$4.57.10^{-10}$	$Pa^{-1}$
Kinematic viscosity	$\nu$	$1 \times 10^{-6}$	$Pa.s$
Thermal conductivity	$k_{th}$	0.6	$W.m^{-1}.K^{-1}$
Heat capacity	$C_p$	4180	$J.kg^{-1}.K^{-1}$
Thermal expansion coeff.	$\alpha$	$0.17 \times 10^{-3}$	$K^{-1}$
Thermal diffusivity	$D_{th}$	$1.43 \times 10^{-7}$	$m^2.s^{-1}$
Prandtl number <sup>b</sup>	$P_r$	7.5	
Grashof number <sup>c</sup>	$G_r$	8.5	
Rayleigh number <sup>d</sup>	$R_a$	76	

305 a rectangular domain (cross-section of the cavity). The side walls are made of aluminium,  
306 while the bottom wall is made of silicon and the upper wall is made of quartz. The simplified  
307 computational domain is then rectangular with a width  $w = 4$  mm and height  $h = 400$   $\mu\text{m}$ .

308 As the PZT used in the experiments has a smaller diameter than the overall cylindrical  
309 cavity, we define an "active area" of width  $w_{ac} = 1$  mm (Fig. 9), where the acoustic force  
310 defined in Eq. 5 is active.

311 We do not simulate acoustic waves emission and reflections in these simulations. The  
312 only acoustic effect is computed as a body force. All solid boundaries are defined as hard  
313 walls with specific thermal properties. A constant temperature is applied to the outer walls  
314 of the cavity, the same way as in the experimental device.

315 We model the aggregate as a set of  $2$   $\mu\text{m}$  diameter beads stuck with each other in the  
316 geometrical center of the resonator (Fig. 9 c)). The position of the aggregate is fixed to  
317 represent the initial condition of a stable aggregate in acoustic levitation just before the  
318 illumination. We don't consider a possible motion of individual particles. The objective is  
319 to compute the possible fluid motions only induced by thermal effects and the acoustic field.

320 We make the hypothesis that the particles absorb the energy injected through the illumi-  
321 nation. This illumination is then modelled through a given heat injected by the aggregate  
322 into the surrounding fluid. The top surface of the aggregate is defined as a constant heat  
323 output flux, and its bottom boundary is thermally insulated. This way we try to take into  
324 account the fact that the aggregates are illuminated from the top. Changing this condition  
325 to set both the top and bottom boundaries of the particles to be heated did not change the  
326 output of the simulation.

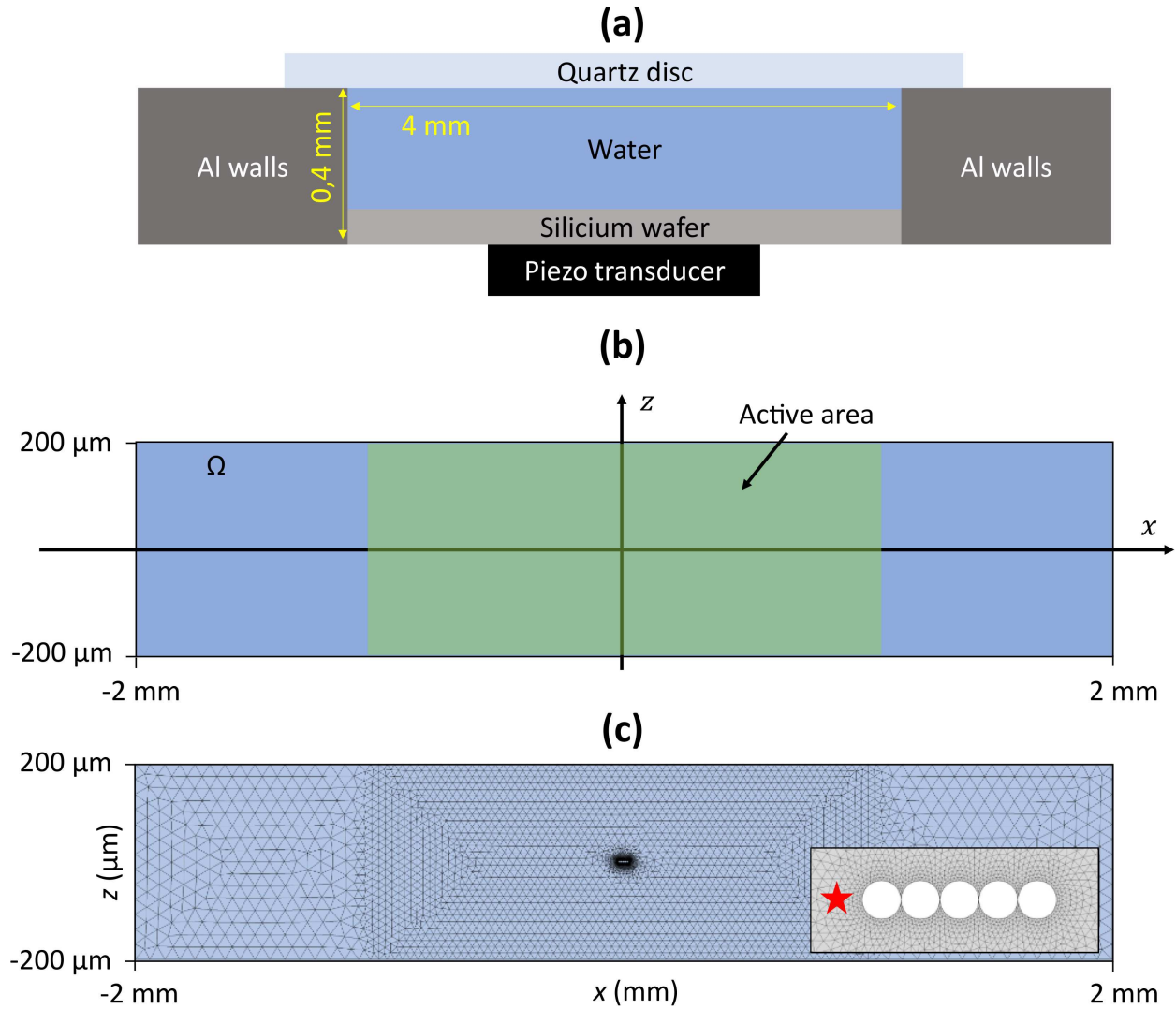


FIG. 9. a) Cross-section of the model acoustophoretic resonator used in his work. It is a cylindrical aluminium cavity, with a silicone wafer as a transmitter layer, on which a PZT element is glued. The reflecting layer is a quartz lid, which is both a good acoustic reflector and a good optical transmitter. b) The corresponding two dimensional computational domain  $\Omega$ . The fluid cavity is closed by rigid walls with specific thermal properties. To account for the fact that the PZT is smaller than the cavity, a subdomain in which the acoustic force is applied is created. It is called the "active area". (c) The aggregate is modelled as a raft of five  $2 \mu\text{m}$  beads fixed in the middle of the cavity, in a similar position as in the acoustic levitation case. On the right part of the figure we added a zoom of the mesh around the beads, together with a red star indicating the location of a local probe used to monitor the fluid velocity.

327 For the initial conditions the heat output of the aggregates to a given value, while the  
 328 bulk temperature of the resonator is set to the temperature of the outer walls.

329 To define the proper size of the smallest element of the mesh we evaluate some important  
 330 length scales: the thermal  $\delta_{th}$  and the viscous  $\delta_{visc}$  penetration depths, that can be written  
 331 as:

$$\delta_{th} = \sqrt{\frac{2\gamma D_{th}}{\omega}} \quad \text{and} \quad \delta_{visc} = \sqrt{\frac{2\mu}{\rho_f \omega}} \quad (7)$$

332 leading to  $\delta_{th} = 0.16 \mu\text{m}$  and  $\delta_{visc} = 0.43 \mu\text{m}$  for a 1.875 MHz acoustic field at  $20^\circ\text{C}$ . We  
 333 use these length scales to define the size of the smallest element of the mesh used for these  
 334 simulations.

335 The mesh is conditioned by two parameters. One controls the maximum element size of  
 336 the grid in the bulk, several elements from the simulated aggregate, while the other controls  
 337 the number of elements on the aggregate boundaries, effectively forcing the local density of  
 338 elements in the aggregate vicinity.

339 The first parameter,  $d_{bulk}$ , controls the precision with which the physical fields in the bulk  
 340 will be rendered. The second,  $N_{part}$ , ensures a good coverage of the two length scales around  
 341 the aggregate as defined in Eq. 7.  $d_{bulk}$  is best represented as a fraction of the aggregate  
 342 width, to account for the physics of the problem.  $N_{part}$  is defined as the number of boundary  
 343 elements surrounding a particle. In this case, we use  $2 \mu\text{m}$  particles, leading to an element  
 344 size of  $0.1 \mu\text{m}$  for  $N_{part} = 62$ . The growing factor of the element size from the boundary  
 345 to the bulk has been set to 1.1, ensuring that the elements keep the same size over two  
 346 micrometers, to cover the thermal length scale at least 4 times.

347 In the following, a maximum bulk element  $d_{bulk} = 0.1L_{agg}$  is selected, and a number of  
 348 boundary elements for the aggregate of  $N_{part} = 800$  is kept, resulting in a mesh of  $3.1 \times 10^6$   
 349 elements.

### 350 C. Volume forces

351 The body buoyant forces are represented as a volume force, active over the whole domain  
 352  $\Omega$ , defined as:

$$\mathbf{f}_{buoy} = -\rho_f \times g \mathbf{e}_z \quad (8)$$

353 with  $g$  the standard gravity. It will take into account any density difference effects,  
 354 especially the ones induced by local heating.

355 As mention previously the acoustic force applied on fluids (eq. 5) is taken into account  
 356 only in the active domain described on Fig. 9.

357 As we are interested in thermal effects over a relatively large range of temperature we  
 358 used the temperature dependency for all physical parameters (density, viscosity, thermal  
 359 conductivity, ...) as defined in the Comsol Material Library.

### 360 D. Natural convection

361 We first ran a test simulation on a very classical Rayleigh-Bénard case, where only buoy-  
 362 ancy and gravity were acting on the fluid. One can expect to observe natural convection rolls  
 363 once above the critical Rayleigh number. Nevertheless, we have shown in Section [V A](#) that

364  $R_a^{crit}$  cannot be reached unless an unphysical ( $\Delta T > 100$ ) very large temperature gradient  
 365 is applied in a taller cavity than the one used here.

366 We used a rectangular box, 800  $\mu\text{m}$  tall and 400  $\mu\text{m}$  wide, with hot bottom plate and a  
 367 cold top plate. The other wall were insulated. We did not observe any onset of the convective  
 368 instability, which is coherent with the Rayleigh numbers explored here.

369 Moreover,  $R_a^{crit}$  depends on the lateral confinement of the fluid, i.e. on the aspect ratio of  
 370 the simulated box as shown by<sup>34</sup>. The critical Rayleigh number  $R_a^{crit}$  also scales with lateral  
 371 confinement of the flow as  $(h/d)^{435}$ , with  $h$  and  $d$  the height and width of the cavity. In  
 372 our case, it leads to a corrected critical Rayleigh number  $R_a^{crit} \approx 27000$ . It confirms that  
 373 the results of the simulation are correct and that there should not be any convective effect  
 374 inside the cavity.

## 375 VI. THERMO-ACOUSTOFLUIDIC SIMULATIONS

### 376 A. Thermo-acoustofluidic instability

377 In the following, we include in the simulation the acoustic force acting on fluids. The  
 378 acoustic energy for all the simulations is  $\langle E_{ac} \rangle = 10 \text{ J.m}^{-3}$ , which is a standard value for our  
 379 cavities.

380 We show on Fig. 10a the contour plot of fluid flow magnitude, together with vector  
 381 plots of the flow created inside the cavity when the upper part of the aggregate is heated.  
 382 One can clearly see four large re-circulations with a very different organization than the  
 383 Rayleigh-Bénard instability. Two large horizontal velocity area appears on both sides of

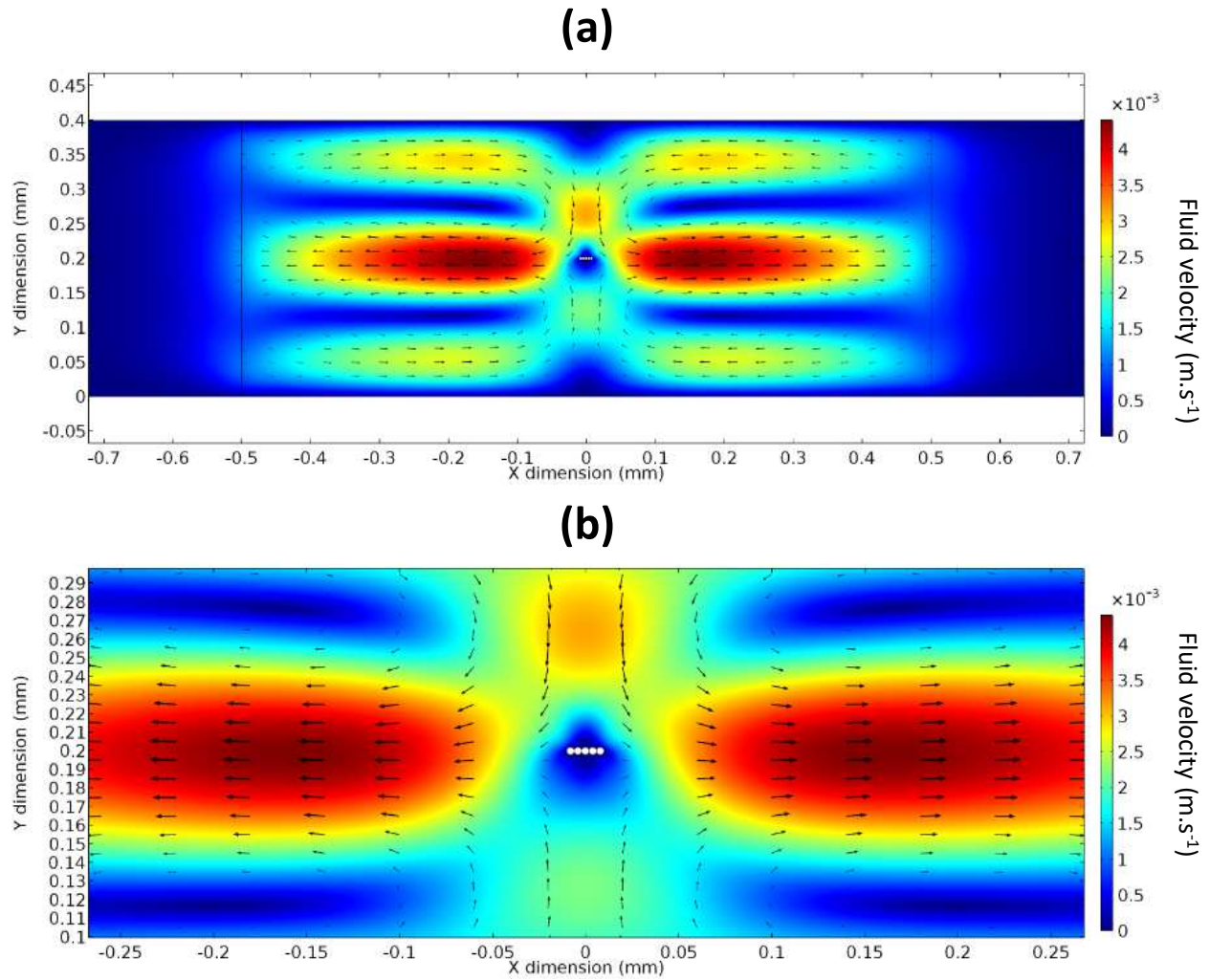


FIG. 10. a) Final steady state of our cavity under the influence of buoyant forces and acoustic forces. The traditional convective recirculation is reversed, and the fluid exits the hot area by the sides, looping back on top and bottom to close the recirculation loops. b) Close-up on the aggregate area, where we can see a slight asymmetry of velocity over and under the aggregate, caused by the fact that this one is rigid. A movie exposing the phenomenon dynamics is available: MM1, this is a file of type "mp4" (2.90Mb).

384 the aggregates. The resulting counter-rotating rolls induce a clear down-flow toward the  
385 aggregate, in the opposite direction of what would be expected for a convective flow.

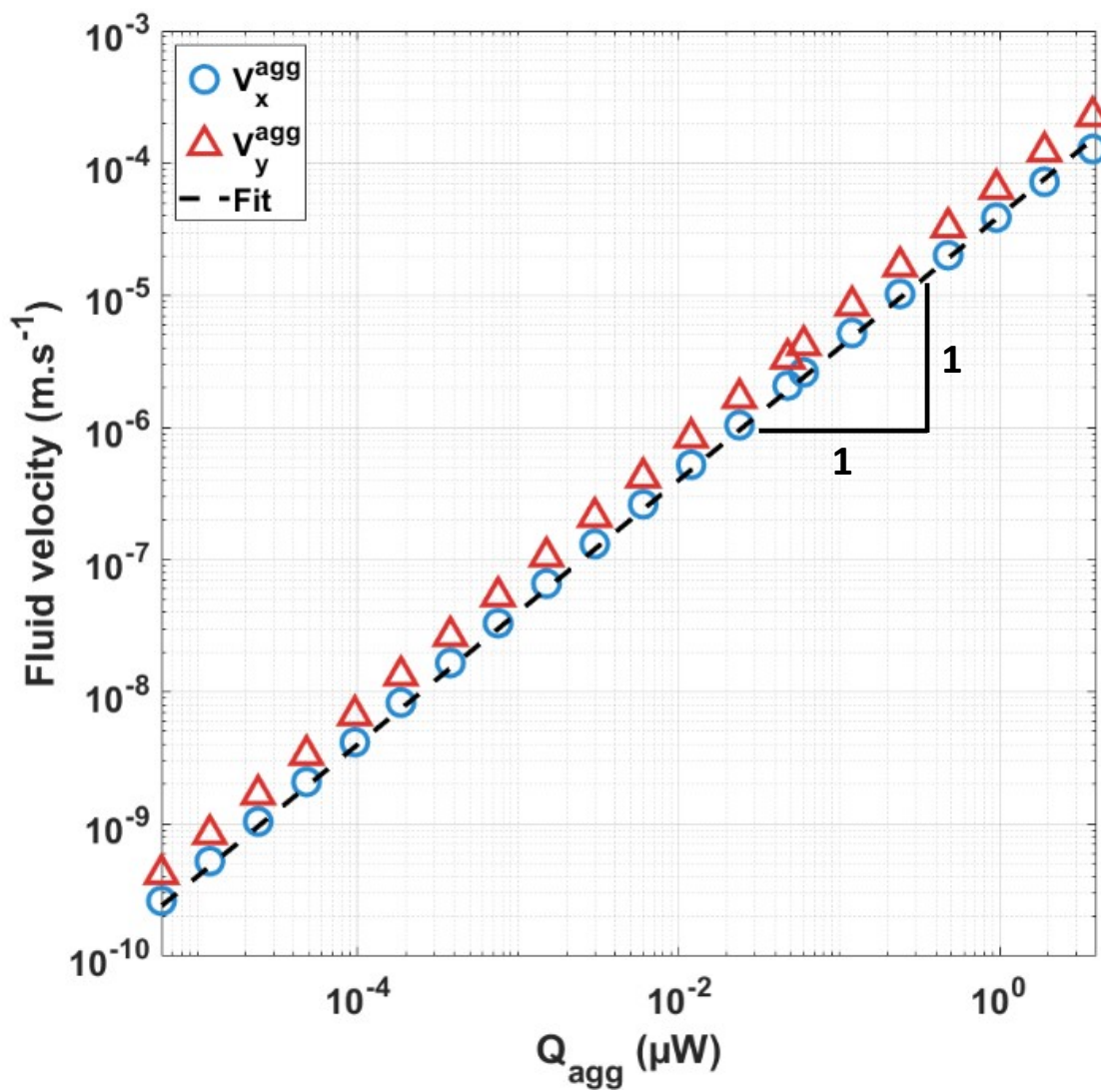
386 This result may look counter-intuitive but it illustrates a very plausible mechanism for  
387 the opto-acoustofluidic effect. Indeed, the particles absorb the light before heating a fluid  
388 layer, which in turns see its density decrease. Instead of moving up as in a classical Rayleigh-  
389 Bénard instability, the fluid is entrained radially by the acoustic force toward the outer walls  
390 of the cavity. Once the lighter fluid exit the active region, the classic mechanism prevails  
391 and the less dense fluid rises toward the upper wall, triggering a large-scale flow inside the  
392 cavity. From this point of view, one can consider this phenomenon as new hydrodynamic  
393 instability, which could be called "thermo-acoustofludic" instability, as it can trigger the  
394 creation of large-scale rotating flows opposite to classic Rayleigh-Bénard instability.

395 This mechanism is compatible with several key properties of the optically induced particle  
396 ejection. It exhibits a fluid motion that can explain the particles ejection from the aggregate  
397 periphery. Indeed, in this simulations the aggregate is fixed, so that the heated layer are  
398 radially ejected. In the experiment particles are in levitation and can be dragged by the  
399 Stokes force induced by this acoustically forced fluid motion. Moreover the fluid motion is  
400 centered on the levitation plane, which explains why the particles are radially ejected and  
401 kept inside the levitation plane.

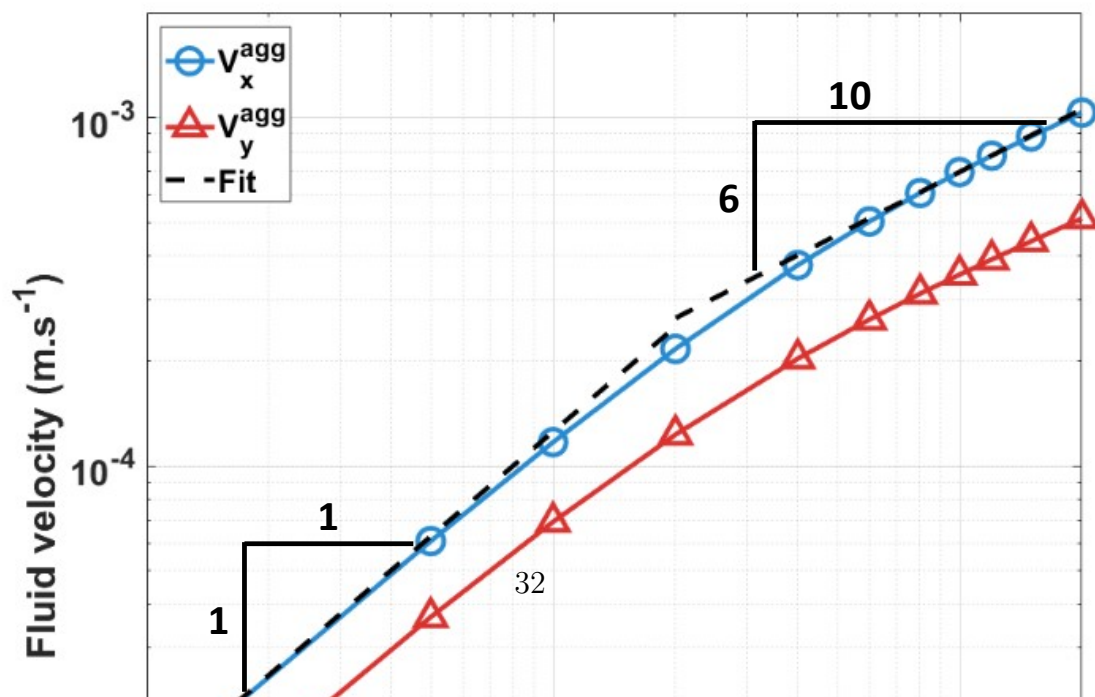
## 402 **B. Scaling of the fluid ejection velocity**

403 We made a parametric study to evaluate the influence of both the acoustic energy and  
404 the thermal heating of the fluid ejection velocity. The fluid velocity is monitored on the

(a)



(b)



405 local probe, on the aggregate side, as shown on Fig. 9 (c). The fluid ejection velocity can  
 406 then be plotted as a function of the heat output (Fig. 11a) and of the acoustic energy (on  
 407 Fig. 11b).

408 We find a positive scaling of the fluid velocity when increasing both the illumination  
 409 power and the acoustic energy of the field, which matches our observations. Even more, the  
 410 scaling is in good agreement with what we found in experiments with very small particles,  
 411 which are very prone to follow fluid motion: a linear scaling for increasing illumination  
 412 power, and a fraction power law with the acoustic energy. Fluid velocity evolution with the  
 413 acoustic energy increase only has a tangential linear evolution at the origin of this graph,  
 414 and a 3/5 scaling, close to the 3/4 scaling found in the previous experimental study<sup>1</sup>.

### 415 C. Ejection velocity of particles

416 As mentioned previously, the numerical simulations were used to demonstrate that a fluid  
 417 flow could be triggered if both thermal effect and acoustic force applied on fluids of different  
 418 densities are taken into account. A possible explanation of the opto-acoutofluidic effect is  
 419 then the entrainment of particles by the ejected fluid. In this case, we have to take into  
 420 account two important effects which will make the particle ejection velocity different from  
 421 the fluid ejection velocity: first, the Stokes drag which will slow the particles and, second,  
 422 the transverse component of the ARF, which will also slow the particle down.

423 Balancing the forces applied to the particles lead to the following equation:

$$\rho_p V_p \frac{\partial \mathbf{u}_p}{\partial t}(x, y) = \mathbf{F}_T + \mathbf{F}_{Stokes} \quad (9)$$

424 where  $V_p$  is the volume of the particle,  $F^{rad}$  the radiation force and  $F_{Stokes}$  the Stokes  
 425 force applied to the moving particle. It leads to the following equation in the levitation  
 426 plane:

$$\begin{aligned} \frac{\partial \mathbf{u}_p}{\partial t}(x, y) + \frac{3\pi\eta d_p}{V_p \rho_p} \times \mathbf{u}_p(x, y) = \\ \frac{1}{\rho_p V_p} (\mathbf{F}_T(x, y) + 3\pi\eta d_p \mathbf{U}_f) \end{aligned} \quad (10)$$

427 where  $\mathbf{F}_{rad}^{radial}$  is the transverse component of the ARF. The solution of a simple first  
 428 degree differential equation of the kind  $y' + ay = b$  being of the form  $y = -b/a \times (e^{-at} - 1)$ ,  
 429 a general solution for these equations can be:

$$\begin{aligned} \mathbf{u}_p(t, x, y) = \frac{\mathbf{F}_T(x, y) + 3\pi\eta d_p \mathbf{U}_f}{3\pi\eta d_p} \\ \times \left[ 1 - \exp\left(-\frac{3\pi\eta d_p}{V_p \rho_p} t\right) \right] \end{aligned} \quad (11)$$

430 Using this relation, we can go further and try to build a phase diagram showing how the  
 431 ejection velocity of the particle depends on the illumination power and acoustic energy. To  
 432 do so we first have to define a value for the transverse component of the ARF  $F_{rad}^{radial}$ . We  
 433 set it to  $10^{-8}$  N, which is quite high (usually around  $10^{-12}$  N in the literature<sup>28,29</sup>), meaning  
 434 that our simulation covered a larger range of optical power than our experiment. Then we  
 435 used the horizontal fluid velocity obtained through the simulations, right at the aggregate  
 436 side, and plugged it into Eq. 11 to translate it into particle ejection velocity.

437 The result of our simulation can be found on Fig. 12, which is a phase diagram showing  
 438 the dependency of the ejection velocity of the particles to both the acoustic energy and

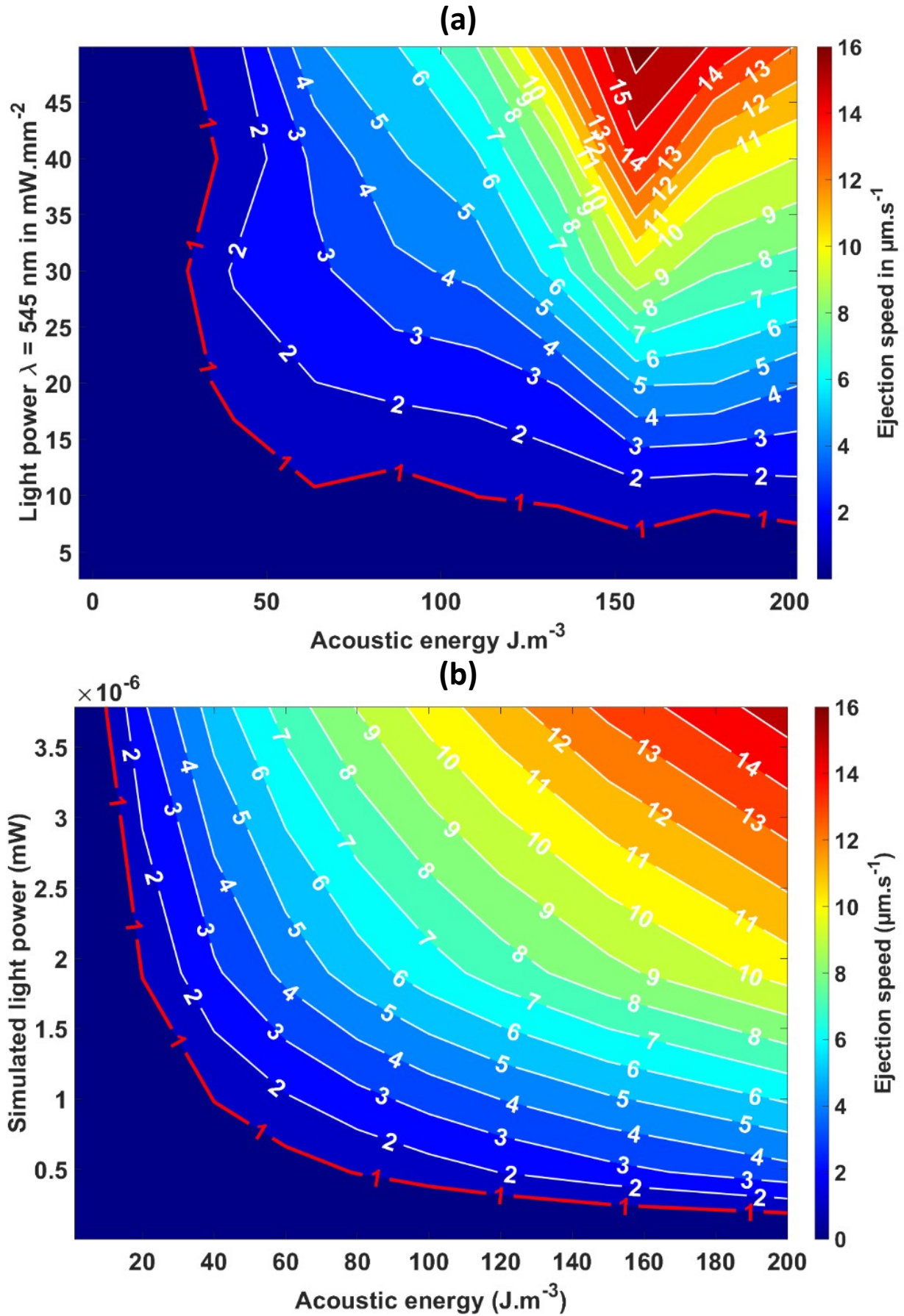


FIG. 12. Phase diagram reconstruction based on the fluid ejection velocity found in the numerical

439 illumination power. It is strikingly similar to the experimental one found in<sup>1</sup>. The cou-  
440 pled effect of the illumination power and the acoustic energy is well recovered, with a very  
441 similar frontier under which no ejection occurs. It proves that our hypothesis are indeed  
442 a plausible explanation for the opto-acoustofluidic effect, which would then be related a  
443 acousto-thermofluidic instability of the fluid.

444 However, one important step remains unclear, which is the exact mechanism leading to  
445 the energy conversion, from the optical power to the eventual heating of the surrounding fluid  
446 layer by the particles or aggregate. The simple absorption spectra of the dye or fluorophore  
447 contained in the particles do not fit with the specific wavelength for which the expulsion is  
448 observed. A more complex coupling with the materials is expected, or a possible effect at  
449 the scale of the particle which is both vibrating because of the acoustic wave and absorbing  
450 energy injected by the monochromatic illumination.

## 451 VII. CONCLUSION

452 We have explored in this study the role of thermal effects on the recently discovered "opto-  
453 acoustofluidic" effect<sup>1</sup>, which leads to the rapid ejection of particles in acoustic levitation  
454 when illuminated at specific optical wavelength.

455 First, we have shown experimentally that for a given acoustic field, optic wave and parti-  
456 cle set, the ejection velocity of the particles is decreasing with increasing temperature. For  
457 temperatures higher than a critical threshold, the particles or aggregates in acoustic levita-  
458 tion are no longer ejected when illuminated. If this experiment demonstrate that there is

indeed a thermal effect, it can not be a simple convection effect. Indeed, we verified that the Rayleigh-Bénard instability can not be triggered in our experiment.

We went further using numerical simulation taking into account both thermal effects and acoustic radiation force on the heated fluid. We found out that the introduction of fluid density gradients through the aggregate heating could trigger lateral jets. The numerical simulations demonstrate the existence of a fluid instability, which we qualified as "thermo-acoustofluidic". If a fluid is locally heated and, at the same time, undergoes an acoustic radiation force, then a large scale flow is triggered, similar to Rayleigh-Bénard convection rolls but with an inverse rotating motion.

The following hypothesis was then that the particles could be dragged away by the induced flow. Ejection of the particles can thus be understood as a competition between a Stokes drag induced by the fluid motion and the transverse component of the ARF applied to the particles. The simulation yields results that are in very good agreement with the characterization made earlier; especially the coupling between acoustic energy and optical power is recovered leading to a very similar phase diagram as the experimental one<sup>1</sup>.

There are many potential applications for this phenomenon. Indeed, if the postulated heating mechanism is confirmed, then any optically absorbing material set in a standing acoustic field could be turned into a local jet generator when illuminated with the adequate wavelength. Should it be levitating particles or a piece of material set at the right position, the density gradient generated will undergo the acoustic effects and be moved like the particles in our study, allowing for elaborate selective contactless manipulation of particles or cells.

481 **ACKNOWLEDGMENTS**

482 We acknowledge the École Doctorale Frontières de l’Innovation en Recherche et Éducation  
483 (ED FIRE), Programme Bettencourt, and the Bettencourt-Schueller Foundation for their  
484 financial support to Gabriel Dumy’s PhD thesis.

485 **REFERENCES**

- 486 <sup>1</sup>G. Dumy, M. Hoyos, and J.-L. Aider, “Observation of selective optical manipulation of  
487 particles in acoustic levitation,” *The Journal of the Acoustical Society of America* **146**(6),  
488 4557–4568 (2019).
- 489 <sup>2</sup>D. Zhou, Y. Gao, J. Yang, Y. C. Li, G. Shao, G. Zhang, T. Li, and L. Li, “Light-ultrasound  
490 driven collective “firework” behavior of nanomotors,” *Advanced Science* **5**(7), 1800122  
491 (2018).
- 492 <sup>3</sup>A. Ashkin, J. M. Dziedzic, J. Bjorkholm, and S. Chu, “Observation of a single-beam  
493 gradient force optical trap for dielectric particles,” *Optics letters* **11**(5), 288–290 (1986).
- 494 <sup>4</sup>A. Ashkin, “History of optical trapping and manipulation of small-neutral particle, atoms,  
495 and molecules,” *IEEE Journal of Selected Topics in Quantum Electronics* **6**(6), 841–856  
496 (2000) <http://ieeexplore.ieee.org/document/902132/> doi: 10.1109/2944.902132.
- 497 <sup>5</sup>J. Wu, “Acoustical tweezers,” *The Journal of the Acoustical Society of America* **89**(5),  
498 2140–2143 (1991).
- 499 <sup>6</sup>J. Wu, “Acoustic radiation force and acoustical tweezers used in biomedical research,” *The*  
500 *Journal of the Acoustical Society of America* **93**(4), 2329–2329 (1993).

- 501 <sup>7</sup>G. Whitworth, M. Grundy, and W. Coakley, “Transport and harvesting of suspended  
502 particles using modulated ultrasound,” *Ultrasonics* **29**(6), 439–444 (1991).
- 503 <sup>8</sup>D. Hartono, Y. Liu, P. L. Tan, X. Y. S. Then, L.-Y. L. Yung, and K.-M. Lim, “On-  
504 chip measurements of cell compressibility via acoustic radiation,” *Lab on a Chip* **11**(23),  
505 4072–4080 (2011).
- 506 <sup>9</sup>L. Puskar, R. Tuckermann, T. Frosch, J. Popp, V. Ly, D. McNaughton, and B. R. Wood,  
507 “Raman acoustic levitation spectroscopy of red blood cells and plasmodium falciparum  
508 trophozoites,” *Lab on a Chip* **7**(9), 1125–1131 (2007).
- 509 <sup>10</sup>B. R. Wood, P. Heraud, S. Stojkovic, D. Morrison, J. Beardall, and D. McNaughton, “A  
510 portable raman acoustic levitation spectroscopic system for the identification and environ-  
511 mental monitoring of algal cells,” *Analytical chemistry* **77**(15), 4955–4961 (2005).
- 512 <sup>11</sup>K. Chen, M. Wu, F. Guo, P. Li, C. Y. Chan, Z. Mao, S. Li, L. Ren, R. Zhang, and  
513 T. J. Huang, “Rapid formation of size-controllable multicellular spheroids via 3d acoustic  
514 tweezers,” *Lab on a Chip* **16**(14), 2636–2643 (2016).
- 515 <sup>12</sup>F. Guo, Z. Mao, Y. Chen, Z. Xie, J. P. Lata, P. Li, L. Ren, J. Liu, J. Yang, M. Dao, *et al.*,  
516 “Three-dimensional manipulation of single cells using surface acoustic waves,” *Proceedings*  
517 *of the National Academy of Sciences* **113**(6), 1522–1527 (2016).
- 518 <sup>13</sup>C. Bouyer, P. Chen, S. Güven, T. T. Demirtaş, T. J. Nieland, F. Padilla, and U. Demirci,  
519 “A bio-acoustic levitational (bal) assembly method for engineering of multilayered, 3d  
520 brain-like constructs, using human embryonic stem cell derived neuro-progenitors,” *Ad-  
521 vanced Materials* **28**(1), 161–167 (2016).

522 <sup>14</sup>S. Gutiérrez-Ramos, M. Hoyos, and J. Ruiz-Suárez, “Induced clustering of escherichia coli  
523 by acoustic fields,” *Scientific reports* **8**(1), 1–8 (2018).

524 <sup>15</sup>A. Garbin, I. Leibacher, P. Hahn, H. Le Ferrand, A. Studart, and J. Dual, “Acoustophoresis  
525 of disk-shaped microparticles: A numerical and experimental study of acoustic radiation  
526 forces and torques,” *The Journal of the Acoustical Society of America* **138**(5), 2759–2769  
527 (2015).

528 <sup>16</sup>W. Wang, L. A. Castro, M. Hoyos, and T. E. Mallouk, “Autonomous motion of metallic  
529 microrods propelled by ultrasound,” *ACS nano* **6**(7), 6122–6132 (2012).

530 <sup>17</sup>S. Ahmed, D. T. Gentekos, C. A. Fink, and T. E. Mallouk, “Self-Assembly of Nanorod  
531 Motors into Geometrically Regular Multimers and Their Propulsion by Ultrasound,” *ACS*  
532 *Nano* **8**(11), 11053–11060 (2014) <https://pubs.acs.org/doi/10.1021/nn5039614> doi:  
533 [10.1021/nn5039614](https://pubs.acs.org/doi/10.1021/nn5039614).

534 <sup>18</sup>S. Ahmed, W. Wang, L. Bai, D. T. Gentekos, M. Hoyos, and T. E. Mallouk, “Density and  
535 Shape Effects in the Acoustic Propulsion of Bimetallic Nanorod Motors,” *ACS Nano* **10**(4),  
536 4763–4769 (2016) <http://pubs.acs.org/doi/10.1021/acsnano.6b01344> doi: [10.1021/  
537 acsnano.6b01344](https://pubs.acs.org/doi/10.1021/acsnano.6b01344).

538 <sup>19</sup>D. Ahmed, T. Baasch, B. Jang, S. Pane, J. Dual, and B. J. Nelson, “Artificial Swim-  
539 mers Propelled by Acoustically Activated Flagella,” *Nano Letters* **16**(8), 4968–4974  
540 (2016) <http://pubs.acs.org/doi/10.1021/acs.nanolett.6b01601> doi: [10.1021/acs.  
541 nanolett.6b01601](https://pubs.acs.org/doi/10.1021/acs.nanolett.6b01601).

- 542 <sup>20</sup>G. Dumy, N. Jeger-Madiot, X. Benoit-Gonin, T.E. Mallouk, M. Hoyos, and J-L. Aider,  
 543 “Acoustic manipulation of dense nanorods in microgravity,” *Microgravity Science and*  
 544 *Technology* **32**(6), 1159–1174 (2020) [https://link.springer.com/article/10.1007/](https://link.springer.com/article/10.1007/s12217-020-09835-7)  
 545 [s12217-020-09835-7](https://link.springer.com/article/10.1007/s12217-020-09835-7) doi: [10.1007/s12217-020-09835-7](https://doi.org/10.1007/s12217-020-09835-7).
- 546 <sup>21</sup>I. Leibacher, W. Dietze, P. Hahn, J. Wang, S. Schmitt, and J. Dual, “Acoustophore-  
 547 sis of hollow and core-shell particles in two-dimensional resonance modes,” *Microflu-*  
 548 *idics and Nanofluidics* **16**(3), 513–524 (2014) [http://link.springer.com/10.1007/](http://link.springer.com/10.1007/s10404-013-1240-7)  
 549 [s10404-013-1240-7](http://link.springer.com/10.1007/s10404-013-1240-7) doi: [10.1007/s10404-013-1240-7](https://doi.org/10.1007/s10404-013-1240-7).
- 550 <sup>22</sup>J. Leão-Neto, J. Lopes, and G. Silva, “Core-Shell Particles that are Unresponsive to Acous-  
 551 tic Radiation Force,” *Physical Review Applied* **6**(2) (2016) [https://link.aps.org/doi/](https://link.aps.org/doi/10.1103/PhysRevApplied.6.024025)  
 552 [10.1103/PhysRevApplied.6.024025](https://link.aps.org/doi/10.1103/PhysRevApplied.6.024025) doi: [10.1103/PhysRevApplied.6.024025](https://doi.org/10.1103/PhysRevApplied.6.024025).
- 553 <sup>23</sup>L. P. Gor’kov, “On the forces acting on a small particle in an acoustical field in an ideal  
 554 fluid,” *Soviet Physics - Doklady* 773–775 (1962).
- 555 <sup>24</sup>F. Mitri, “Acoustic radiation force acting on elastic and viscoelastic spherical shells placed  
 556 in a plane standing wave field,” *Ultrasonics* **43**(8), 681–691 (2005) [http://linkinghub.](http://linkinghub.elsevier.com/retrieve/pii/S0041624X05000090)  
 557 [elsevier.com/retrieve/pii/S0041624X05000090](http://linkinghub.elsevier.com/retrieve/pii/S0041624X05000090) doi: [10.1016/j.ultras.2005.03.](https://doi.org/10.1016/j.ultras.2005.03.002)  
 558 [002](https://doi.org/10.1016/j.ultras.2005.03.002).
- 559 <sup>25</sup>M. Settnes and H. Bruus, “Forces acting on a small particle in an acoustical field in a  
 560 viscous fluid,” *Physical Review E* **85**(1) (2012) [https://link.aps.org/doi/10.1103/](https://link.aps.org/doi/10.1103/PhysRevE.85.016327)  
 561 [PhysRevE.85.016327](https://link.aps.org/doi/10.1103/PhysRevE.85.016327) doi: [10.1103/PhysRevE.85.016327](https://doi.org/10.1103/PhysRevE.85.016327).

- 562 <sup>26</sup>A. A. Doinikov, “Acoustic radiation pressure on a compressible sphere in a viscous fluid,”  
 563 Journal of Fluid Mechanics **267**(-1), 1 (1994) [http://www.journals.cambridge.org/](http://www.journals.cambridge.org/abstract_S0022112094001096)  
 564 [abstract\\_S0022112094001096](http://www.journals.cambridge.org/abstract_S0022112094001096) doi: [10.1017/S0022112094001096](https://doi.org/10.1017/S0022112094001096).
- 565 <sup>27</sup>G. Dumy, X. Benoit-Gonin, M. Hoyos, and J.-L. Aider, “Acoustic propulsion of metallic  
 566 nano-cylinders: contribution of the local vertical acceleration from micro to hyper gravity,”  
 567 (2019).
- 568 <sup>28</sup>T. Tuziuti, T. Kozuka, and H. Mitome, “Measurement of distribution of acoustic radiation  
 569 force perpendicular to sound beam axis,” Japanese journal of applied physics **38**(5S), 3297  
 570 (1999).
- 571 <sup>29</sup>S. M. Woodside, B. D. Bowen, and J. M. Piret, “Measurement of ultrasonic forces for  
 572 particle–liquid separations,” AIChE journal **43**(7), 1727–1736 (1997).
- 573 <sup>30</sup>J. T. Karlsen, P. Augustsson, and H. Bruus, “Acoustic Force Density Acting on Inho-  
 574 mogeneous Fluids in Acoustic Fields,” Physical Review Letters **117**(11) (2016) [https://](https://link.aps.org/doi/10.1103/PhysRevLett.117.114504)  
 575 [link.aps.org/doi/10.1103/PhysRevLett.117.114504](https://link.aps.org/doi/10.1103/PhysRevLett.117.114504) doi: [10.1103/PhysRevLett.](https://doi.org/10.1103/PhysRevLett.117.114504)  
 576 [117.114504](https://doi.org/10.1103/PhysRevLett.117.114504).
- 577 <sup>31</sup>O. Dron and J.-L. Aider, “Acoustic energy measurement for a standing acoustic wave in  
 578 a micro-channel,” EPL (Europhysics Letters) **97**(4), 44011 (2012) [http://stacks.iop.](http://stacks.iop.org/0295-5075/97/i=4/a=44011?key=crossref.31b8ebc628fc2d2a9fb8ea61696bb8a0)  
 579 [org/0295-5075/97/i=4/a=44011?key=crossref.31b8ebc628fc2d2a9fb8ea61696bb8a0](http://stacks.iop.org/0295-5075/97/i=4/a=44011?key=crossref.31b8ebc628fc2d2a9fb8ea61696bb8a0)  
 580 doi: [10.1209/0295-5075/97/44011](https://doi.org/10.1209/0295-5075/97/44011).
- 581 <sup>32</sup>N. T. Ouellette, H. Xu, and E. Bodenschatz, “A quantitative study of three-dimensional  
 582 lagrangian particle tracking algorithms,” Experiments in Fluids **40**(2), 301–313 (2006).

583 <sup>33</sup>N. T. Ouellette, “Particle-based measurement techniques for soft matter,” *Experimental*  
584 *and Computational Techniques in Soft Condensed Matter Physics* 180 (2010).

585 <sup>34</sup>M. Krishnan, V. M. Ugaz, and M. A. Burns, “Pcr in a rayleigh-benard convection  
586 cell.(biochemistry),” *Science* **298**(5594), 793–794 (2002).

587 <sup>35</sup>R. Muddu, Y. A. Hassan, and V. M. Ugaz, “Chaotically accelerated polymerase chain  
588 reaction by microscale rayleigh–bénard convection,” *Angewandte Chemie International*  
589 *Edition* **50**(13), 3048–3052 (2011).